Optics Letters

Tunable hybrid silicon nitride and thin-film lithium niobate electro-optic microresonator

ABU NAIM R. AHMED,[1,*] SHOUYUAN SHI,[1] MATHEW ZABLOCKI,[1] PENG YAO,[2] AND DENNIS W. PRATHER[1]

[1]*School of Electrical and Computer Engineering, University of Delaware, Newark, Delaware 19716, USA*
[2]*Phase Sensitive Innovations, Newark, Delaware 19711, USA*
Corresponding author: naimece@udel.edu

This Letter presents, to the best of our knowledge, the first hybrid Si_3N_4-$LiNbO_3$-based tunable microring resonator where the waveguide is formed by loading a Si_3N_4 strip on an electro-optic (EO) material of X-cut thin-film $LiNbO_3$. The developed hybrid Si_3N_4-$LiNbO_3$ microring exhibits a high intrinsic quality factor of 1.85×10^5, with a ring propagation loss of 0.32 dB/cm, resulting in a spectral linewidth of 13 pm, and a resonance extinction ratio of ~27 dB within the optical C-band for the transverse electric mode. Using the EO effect of $LiNbO_3$, a 1.78 pm/V resonance tunability near 1550 nm wavelength is demonstrated. © 2019 Optical Society of America

https://doi.org/10.1364/OL.44.000618

Modern technology has stepped into the era of the Internet of Things (IoT), on-chip data centers, superconducting quantum computers, artificial intelligence (AI), 5G networks, etc., of which all these next-generation technologies demand low drive power, ultrawide bandwidth, high-speed data transmission, small footprint, and a complementary metal-oxide-semiconductor (CMOS)-compatible fabrication process. Capable of simultaneously addressing these challenges, optical interconnect has generated great interest in recent years [1–6]. Accordingly, the microring resonator is considered a key building block of an optical interconnect fabric, as it is essential for all-optical switching, high-speed modulation, tunable optical filters, optical frequency comb generation, laser resonators, compact footprint, etc. [7]. Historically, microring resonators have been widely investigated in different material systems including Si [7–9], Si_3N_4 [9,10], graphene-Si [11], $LiNbO_3$ [12–16], Si-$LiNbO_3$ [17–20], Si-GaN [21], InP [22], AlN [23], GaAs [24], polymers [25], chalcogenide [26], etc. The tuning methods explored in these materials include the plasma dispersion effect, the thermo-optic effect, the electro-absorption effect, electro-optomechanics, and the electro-optic (EO) effect [12,17,26,27]. Unfortunately, many of them suffer from drawbacks and limitations including low modulation bandwidth, low extinction ratio, temperature sensitivity, nonlinearity, low modulation efficiency, aging, stability, scalability, and large footprint [12,14,23,26,27]. Recently the crystal-ion-sliced (CIS) thin-film $LiNbO_3$ on insulator

(LNOI) platform has excited a lot of attention due to its superior advantages, such as tight optical mode confinement, high EO modulation efficiency, linear voltage–index relationship, ultrawide operational bandwidth, low drive power, high extinction ratio, and small bending radii [16–19,28–30]. Both standalone and hybrid $LiNbO_3$ platforms (e.g., Si-$LiNbO_3$, Si_3N_4-$LiNbO_3$) [28–33] are very active in the related research fields. While most recent work has successfully demonstrated a low optical loss in standalone $LiNbO_3$ by the plasma-etching method [13,14] to form waveguide guiding, the hybrid platform still remains as an open research field owning its potential hybrid integration with the CMOS-compatible manufacturing process and driving circuitry. Moreover, $LiNbO_3$ is a material that presents difficulties when trying to etch, so the etch processes of $LiNbO_3$ are still underdeveloped compared to those in silicon-based materials. The hybrid platform circumvents this difficulty by utilizing a more conventional film and etch of silicon-based materials to enabling waveguiding in a $LiNbO_3$, without the requirement of etching the $LiNbO_3$ itself. Previously, hybrid Si-$LiNbO_3$-based microring resonators have been extensively reported in the literature [18–21]. Microring devices based on the Si_3N_4-$LiNbO_3$ material have yet to be studied. Si_3N_4-$LiNbO_3$ comes forward as a promising material system due to better index matching, high mode confinement inside $LiNbO_3$ [32–34], the ultralow propagation loss of Si_3N_4, high power handling capabilities, Si_3N_4 insulating properties, and a wide optical transparency window [35]. Previous Si_3N_4-$LiNbO_3$-based work focuses primarily on passive devices with vertical mode transition structures from Si_3N_4 to $LiNbO_3$ material [32,33] and push–pull Mach-Zehnder interferometer (MZI) modulation [34]. Furthermore, most of the prior hybrid material systems were realized by bonding LNOI onto the strip-loaded waveguide structure [18,28,31–33], which is challenging due to reliability, fabrication, and design complexity (handle removal), and electrode fabrication process.
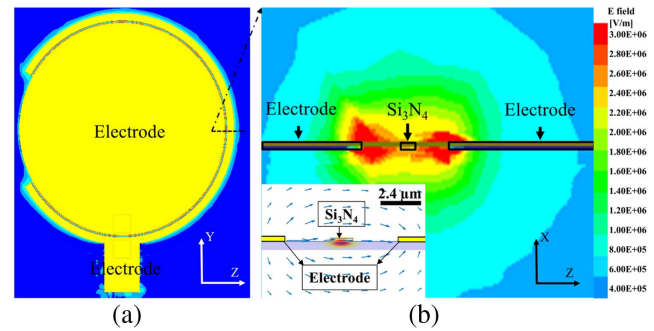
In this Letter, the first hybrid Si_3N_4-$LiNbO_3$-based high-Q active microring resonator is presented, where plasma-enhanced chemical vapor deposition (PECVD) Si_3N_4 thin film was directly deposited on an LNOI wafer to define the strip-loaded waveguide structure, eliminating the postfabrication
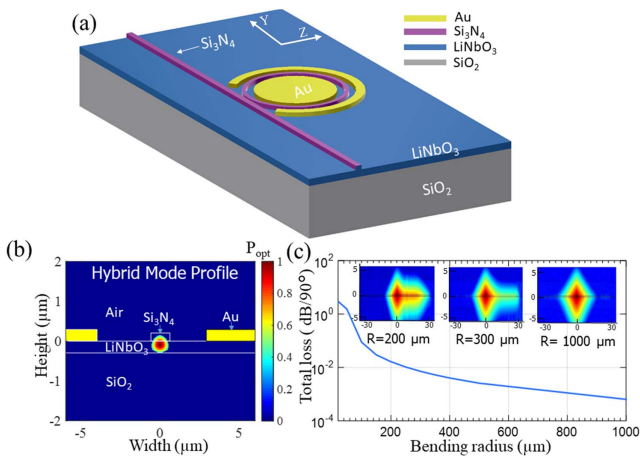
Fig. 1. (a) Schematic of the tunable hybrid Si_3N_4-$LiNbO_3$ microring resonator with integrated electrodes (not drawn in scale). (b) Simulated TE mode field profile of a hybrid Si_3N_4-$LiNbO_3$ waveguide formed by a 200 nm × 1.2 μm Si_3N_4 loading strip at 1550 nm. (c) Simulated bending loss as a function of bending radius for the TE mode. The bending loss is presented as decibel (dB) per 90° bend.

Fig. 2. (a) Simulated electric field distribution of the microring with 10 V voltage applied between the ground signal electrodes. (b) The electric field distribution in the cross section indicates the field concentration near 2 MV/m under the Si_3N_4 strip waveguide. The inset shows the simulated RF electric field direction (arrows) of the device's cross section.

processes, such as bonding and handle removal. The device consists of a microring and a coupled straight bus waveguide, exhibiting high intrinsic Q-factors of 1.8×10^5 with a small resonant linewidth of 13 pm. The measured extinction ratio and ring loss are ~27 dB and 0.32 dB/cm, respectively, near 1550 nm, within the optical C-band. Finally, the EO tuning of the microring is demonstrated, achieving a tunability of 1.78 pm/V.

The schematic of the tunable Si_3N_4-$LiNbO_3$ hybrid microring structure is shown in Fig. 1(a). The cross section illustrated in Fig. 1(b) shows the optical waveguide consisting of a Si_3N_4 strip placed on the top of the 300 nm X-cut thin-film $LiNbO_3$ and a 2 μm SiO_2 bottom cladding layer. The thickness and width of the Si_3N_4 strip are 200 nm and 1.2 μm, respectively, chosen such that they support a single transverse electric (TE)-polarized fundamental mode at a wavelength of 1550 nm. The optimal device dimensions are chosen such that the optical mode is mostly confined in the $LiNbO_3$ and to ensure minimum bending loss. The complete mode confinement factor map in the $LiNbO_3$ (Γ_{LN}) was studied in a previous work [33] using Lumerical software modules. The mode confinement factor in the $LiNbO_3$ is ~65% for the above-mentioned structure. The bending loss for different bend radii is studied using Lumerical Mode Solver shown in Fig. 1(c). At a bending radius of 200 μm, the bending loss is below 0.1 dB/90° bend, though the logarithmic mode profile in the inset shows an asymmetric mode distribution. In this work, a 300 μm bending radius is chosen to ensure bending loss below 0.01 dB/90° bend, and the logarithmic mode profile is closer to the straight waveguide section. The refractive index of the PECVD Si_3N_4 used within the model is 1.94, which is consistent with the experimental value. The final structure consists of a 300 μm ring radius, which is side coupled to a straight bus waveguide. EO tuning of the microring resonator is achieved by patterning signal and ground gold electrodes on the LNOI substrate on both the sides of the optical waveguide for the X-cut $LiNbO_3$ configuration. This configuration offers a strong mode

overlap between the fundamental TE-polarized light and the applied electric field with the $LiNbO_3$ crystal axis. The modulating electrodes are placed around the microring resonator except for the region immediately surrounding the optical coupling section from the bus so that an applied voltage does not impact the coupling between the ring and bus waveguide. The gap between the ground and signal electrodes and the thickness are 7 μm and 250 nm, respectively. The electrode gap is chosen such that it ensures low metal absorption loss and maximum optical and electric field overlap. The simulated electric field distributions for the top view and the cross-sectional view of the structure are shown in Fig. 2(a) and Fig. 2(b), respectively. The simulation is performed by ANSYS high frequency structure simulator (HFSS), and the electric field under the Si_3N_4 waveguide is about 2 MV/m for a 10 V applied voltage. The strong electric field concentration in the $LiNbO_3$ EO material will induce a significant optical index change, and thus efficient EO modulation.
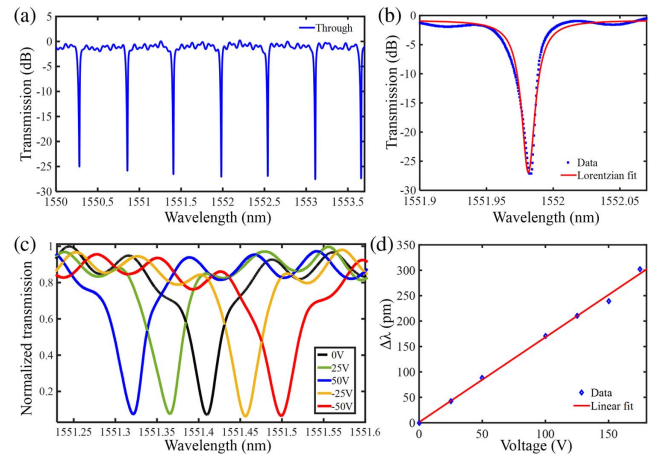
The thin-film CIS LNOI is procured from NanoLN. The $3''$ wafer consists of a 300 nm thick layer of an X-cut $LiNbO_3$ device layer bonded to a 500 μm thick quartz handle wafer via a 2 μm PECVD SiO_2 intermediate layer. The fabrication process of the microring consists of three main steps: PECVD Si_3N_4 deposition, e-beam lithography (EBL) for microring definition, and electrode fabrication. To form the hybrid device, a thin film of a Si_3N_4 layer is deposited on top of the thin-film $LiNbO_3$ using PECVD. Although PECVD Si_3N_4 is lossy compared to the low-pressure chemical vapor deposition (LPCVD) due to the residual hydrogen content, the LPCVD high processing temperature produces cracks in $LiNbO_3$. The optical loss can be further improved by introducing a glass cladding layer or reducing the hydrogen content in the Si_3N_4 by sputtering or other low temperature deposition techniques [36]. A 200 nm of PECVD Si_3N_4 is deposited using the following parameters: $SiH_4/NH_3/N_2$, 10 sccm/6 sccm/300 sccm, a chamber pressure of 100 Pa, RF power of 50 W, and temperature of 300°C. The deposition rate is 42.85 nm/min, and the measured refractive index is 1.943 at 1550 nm. The microring and the waveguide are defined on the Si_3N_4 layer by EBL using a similar process as described in a previous work [33]. The metal electrodes are defined on top of the $LiNbO_3$ layer as a ground signal configuration. A bilayer lift-off process and
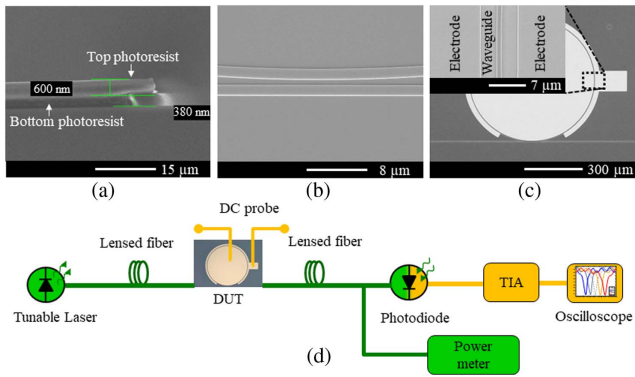
Fig. 3. (a) SEM image of the bilayer lift-off process. (b) SEM image of the microring coupling section. (c) SEM image of a hybrid Si_3N_4-$LiNbO_3$ microring with a bending radius of 300 μm, waveguide thickness of 200 nm, and waveguide width of 1.2 μm. The inset shows the zoomed section of the boxed region. (d) Schematic of the experimental setup for measuring the transmission spectrum and electro-optically tuning the resonant wavelength in the hybrid microring.

Fig. 4. Hybrid microring resonator characterization. (a) The measured transmission spectrum of the passive microring at the through port for TE mode using a tunable laser near the 1550 nm. The free spectral range is 0.58 nm, and the resonance extinction ratios are up to 27 dB. (b) The Lorentz fitting (red curve) of the resonance dip at 1551.98 nm, which corresponds to an intrinsic Q of 1.83×10^5. (c) The resonant spectra as a function of the applied voltage for TE mode at wavelengths near 1551.410 nm (black curve) of a microring resonator; the red and blue curves are the corresponding electro-optically shifted curves by applying a voltage of –50 V and +50 V to the device electrodes, respectively. The measured tunability is 1.78 pm/V. (d) The resonant wavelength shift as a function of the applied DC voltage.

evaporation process are performed to pattern the metal electrode. We use LOR-5A (MicroChem Corp) and AZ MIR 701 (MicroChemicals) photoresists in a positive-tone mode in this bilayer process. The LOR-5A is coated first, followed by the AZ MIR 701 coating. The electrodes are patterned using the laser writer (Heidelberg MLA 100), which maintains high-precision alignment with the microring structure. After lithography, both the resists are developed at the same time using AZ 300 MIF developer. The bilayer lift-off process creates an undercut profile [Fig. 3(a)], which helps to define fine pattern and achieve clean solvent lift-off. A brief plasma descum is performed before metal evaporation to remove photoresist residue and establish good metal adhesion. Next, a 20 nm Ti layer followed by a 250 nm Au layer are deposited via e-beam evaporation. Then the metal lift-off is performed in the NMP solvent (1-methyl-2-pyrrolidinone) at 80°C in the ultrasonic bath. Finally, the device's waveguide facets are diced and polished for fiber–chip coupling. The scanning electron micrograph (SEM) image of the fabricated microring coupling section and the microring with the integrated electrode are shown in Figs. 3(b) and 3(c).

The fabricated hybrid microring resonator is characterized by extracting the transmission spectrum using a Keysight tunable laser swept at wavelengths surrounding 1550. The experimental setup is shown in Fig. 3(d). The tunable laser source is coupled to the device under test (DUT) using a lensed fiber, which is aligned to launch TE-polarized light. The output light is detected and monitored on an oscilloscope with the assistance of a transimpedance amplifier (TIA). The measured transmission spectrum of the single bus microring resonator around 1550 nm is shown in Fig. 4(a). The periodic dips and uniform spacing between adjacent dips indicate that only one mode is present inside the microring. The measured free spectral range (FSR) and the spectral linewidth of the microring are $\Delta\lambda_{FSR} = 0.58 \pm 0.004$ nm and $\delta\lambda_{FWHM} = 0.013 \pm 0.0006$ nm. The maximum potential extinction ratio is about 26.92 dB at 1551.98 nm. The intrinsic quality factor of 1.85×10^5 at 1551.98 nm is extracted by fitting the central transmission

dip with a Lorentzian [37] as shown in Fig. 4(b). The loss per unit length in the ring [37] is calculated as 0.32 dB/cm. The microring resonator tuning ability is characterized by the transmission spectrum shift by applying different voltages to the device electrodes. The applied voltage will change the refractive index of the $LiNbO_3$ due to its EO properties, which causes a phase change and shifts the resonance condition. The experimental setup is the same as Fig. 3(d). The DC bias is applied to the top of the integrated electrodes using a voltage source and DC probe to a ring resonator centered at 1551.410 nm. The bias voltage is varied from +50 V to –50 V to demonstrate wavelength tuning spectra shown in Fig. 4(c). The measured results indicate a total of 178.4 pm wavelength shift when the voltage changes from +50 V to –50 V. Figure 4(d) shows the wavelength shift as a function of the applied voltage, which shows a linear dependence of the wavelength shift on the applied voltage. The measured tuning coefficient is 1.784 pm/V. As a result, only ~7 V driving voltage is required to tune over a spectral range of a spectral width of 13 pm. The tunability can be further improved by reconfiguring the electrode design and microring structure [38,39].

In summary, the presented work demonstrates a high-Q and tunable hybrid microring resonator where a potential photonic platform for future photonic integrated circuit (PIC) based on Si_3N_4 on thin-film $LiNbO_3$ has been explored. This is the first time, to the best of our knowledge, that a hybrid Si_3N_4-$LiNbO_3$-based tunable microring resonator with high-Q has been fabricated and characterized. The fabrication process involved simple PECVD Si_3N_4 deposition on the LNOI and waveguide pattern on Si_3N_4, simplifying electrode

design and fabrication methods. The fabricated microring resonator demonstrated a high intrinsic Q of 1.85×10^5 and resonance extinction ratio of ~27 dB at optical C-band for the TE mode. For the TE mode, microelectrodes are patterned on top of the $LiNbO_3$ surface to tune the microring electro-optically. A 1.78 pm/V tunability of the resonant wavelength and a linear wavelength change ($\Delta\lambda$) voltage relationship were observed. The current work will encourage future research on the development of the Si_3N_4-$LiNbO_3$ platform for the development of complex, high-performance future PIC.

REFERENCES

1. H. Subbaraman, X. Xu, A. Hosseini, X. Zhang, Y. Zhang, D. Kwong, and R. T. Chen, Opt. Express **23**, 2487 (2015).
2. Z. Li, I. Shubin, and X. Zhou, Opt. Express **23**, 3717 (2015).
3. K. Ishii, T. Inoue, and S. Namiki, Proc. SPIE **10131**, 1013105 (2017).
4. M. A. Taubenblatt, in *Photonic Networks and Devices* (Optical Society of America, 2018), paper NeTh3F-2.
5. C. Wang, M. Zhang, X. Chen, M. Bertrand, A. Shams-Ansari, S. Chandrasekhar, P. Winzer, and M. Lončar, Nature **562**, 101 (2018).
6. G. T. Reed, G. Mashanovich, F. Y. Gardes, and D. J. Thomson, Nat. Photonics **4**, 518 (2010).
7. W. Bogaerts, P. De Heyn, T. Van Vaerenbergh, K. De Vos, S. Kumar Selvaraja, T. Claes, P. Dumon, P. Bienstman, D. Van Thourhout, and R. Baets, Laser Photon. Rev. **6**, 47 (2012).
8. P. Dong, W. Qian, H. Liang, R. Shafiiha, N.-N. Feng, D. Feng, X. Zheng, A. V. Krishnamoorthy, and M. Asghari, Opt. Express **18**, 9852 (2010).
9. G. Piccoli, M. Bernard, and M. Ghulinyan, Optica **5**, 1271 (2018).
10. D. J. Blumenthal, R. Heideman, D. Geuzebroek, A. Leinse, and C. Roeloffzen, Proc. IEEE **106**, 2209 (2018).
11. C. Xiang, M. L. Davenport, J. B. Khurgin, P. A. Morton, and J. E. Bowers, IEEE J. Sel. Top. Quantum Electron. **24**, 5900109 (2018).
12. Y. Ding, X. Zhu, S. Xiao, H. Hu, L. H. Frandsen, N. A. Mortensen, and K. Yvind, Nano Lett. **15**, 4393 (2015).
13. M. Mahmoud, L. Cai, C. Bottenfield, and G. Piazza, IEEE Photon. J. **10**, 6600410 (2018).
14. L. Chen, M. G. Wood, and R. M. Reano, Opt. Express **21**, 27003 (2013).
15. J. D. Witmer, J. A. Valery, P. Arrangoiz-Arriola, C. J. Sarabalis, J. T. Hill, and A. H. Safavi-Naeini, Sci. Rep. **7**, 46313 (2017).
16. J. Chiles and S. Fathpour, Optica **1**, 350 (2014).
17. P. Rabiei, J. Ma, S. Khan, J. Chiles, and S. Fathpour, Opt. Express **21**, 25573 (2013).
18. B. Thubthimthong, T. Sasaki, and K. Hane, IEEE Photon. J. **7**, 7801511 (2015).
19. R. Grover, P. P. Absil, V. Van, J. V. Hryniewicz, B. E. Little, O. King, L. C. Calhoun, F. G. Johnson, and P.-T. Ho, Opt. Lett. **26**, 506 (2001).
20. C. Xiong, W. H. Pernice, X. Sun, C. Schuck, K. Y. Fong, and H. X. Tang, New J. Phys. **14**, 095014 (2012).
21. T. A. Ibrahim, V. Van, and P.-T. Ho, Opt. Lett. **27**, 803 (2002).
22. M. Lee, H. E. Katz, C. Erben, D. M. Gill, P. Gopalan, J. D. Heber, and D. J. McGee, Science **298**, 1401 (2002).
23. A. Rao, A. Patil, J. Chiles, M. Malinowski, S. Novak, K. Richardson, P. Rabiei, and S. Fathpour, Opt. Express **23**, 22746 (2015).
24. C. Wang, M. Zhang, B. Stern, M. Lipson, and M. Lončar, Opt. Express **26**, 1547 (2018).
25. A. Rao and S. Fathpour, IEEE J. Sel. Top. Quantum Electron. **24**, 3400114 (2018).
26. A. Guarino, G. Poberaj, D. Rezzonico, R. Degl'Innocenti, and P. Günter, Nat. Photonics **1**, 407 (2007).
27. A. J. Mercante, S. Shi, P. Yao, L. Xie, R. M. Weikle, and D. W. Prather, Opt. Express **26**, 14810 (2018).
28. A. Boes, B. Corcoran, L. Chang, J. Bowers, and A. Mitchell, Laser Photon. Rev. **12**, 1700256 (2018).
29. P. O. Weigel, M. Savanier, C. T. DeRose, A. T. Pomerene, A. L. Starbuck, A. L. Lentine, V. Stenger, and S. Mookherjea, Sci. Rep. **6**, 22301 (2016).
30. L. Chang, M. H. Pfeiffer, N. Volet, M. Zervas, J. D. Peters, C. L. Manganelli, E. J. Stanton, Y. Li, T. J. Kippenberg, and J. E. Bowers, Opt. Lett. **42**, 803 (2017).
31. A. N. R. Ahmed, A. Mercante, S. Shi, P. Yao, and D. W. Prather, Opt. Lett. **43**, 4140 (2018).
32. S. Jin, L. Xu, H. Zhang, and Y. Li, IEEE Photon. Technol. Lett. **28**, 736 (2016).
33. Y. Wang, Z. Chen, L. Cai, Y. Jiang, H. Zhu, and H. Hu, Opt. Mater. Express **7**, 4018 (2017).
34. M. Zhang, C. Wang, R. Cheng, A. Shams-Ansari, and M. Lončar, Optica **4**, 1536 (2017).
35. R. Baets, A. Z. Subramanian, S. Clemmen, B. Kuyken, P. Bienstman, N. Le Thomas, G. Roelkens, D. Van Thourhout, P. Helin, and S. Severi, in *Optical Fiber Communications Conference and Exhibition (OFC)* (IEEE, 2016), pp. 1–3.
36. A. S. Lee, N. Rajagopalan, M. Le, B. H. Kim, and H. M'saad, J. Electrochem. Soc. **151**, F7 (2004).
37. L.-W. Luo, G. S. Wiederhecker, J. Cardenas, C. Poitras, and M. Lipson, Opt. Express **19**, 6284 (2011).
38. M. Zhang, C. Wang, Y. Hu, A. Shams-Ansari, G. Ribeill, M. Soltani, and M. Loncar, in *CLEO: Science and Innovations* (Optical Society of America, 2018), paper SM1I-7.
39. M. Zhang, C. Wang, B. Buscaino, A. Shams-Ansari, J. M. Kahn, and M. Loncar, in *CLEO: QELS_Fundamental Science* (Optical Society of America, 2018), paper FW3E-4.